Nanoscale

A filterless, visible-blind, narrow-band, and near-infrared photodetector with a gain

Liang Shen, Yang Zhang, Yang Bai, Xiaopeng Zheng, Qi Wang and Jinsong Huang*

In many applications of near-infrared (NIR) light detection, a band-pass filter is needed to exclude the noise caused by visible light. Here, we demonstrate a filterless, visible-blind, narrow-band NIR photodetector with a full-width at half-maximum of <50 nm for the response spectrum. These devices have a thick (>4 μm) nanocomposite absorbing layers made of polymer–fullerene:lead sulfide (PbS) quantum dots (QDs). The PbS QDs yield a photoconductive gain due to their hole-trapping effect, which effectively enhances both the responsivity and the visible rejection ratio of the external quantum efficiency by >10 fold compared to those without PbS QDs. Encouragingly, the inclusion of the PbS QDs does not increase the device noise. We directly measured a noise equivalent power (NEP) of 6.1 pW cm^{-2} at 890 nm, and a large linear dynamic range (LDR) over 11 orders of magnitude. The highly sensitive visible-blind NIR narrow-band photodetectors may find applications in biomedical engineering.

1. Introduction

Solution-processed photodetectors made of low-cost organic semiconductors, nanomaterials and hybrid perovskites are rivaling with those made of traditional inorganic semiconductor materials such as GaN, silicon and InGaAs.[1–17] Photodetectors can be classified as broad-band and narrow-band types in terms of their spectral response bandwidth, which is normally consistent with the absorption spectra of the photoactive materials. Generally, broad-band photodetectors have been intensively studied in the past to cover a spectrum as broad as possible, however narrow-band photodetectors, which are required in many applications, have received much less attention. Narrow-band ultraviolet (UV) or infrared (IR) photodetectors with a small full-width at half-maximum (FWHM) are desired in applications where the visible light response needs to be excluded. Visible-blind or even solar-blind photodetectors have been designed using wide band gap semiconductors, such as group-III nitrides.[18] So far, visible-blind near-infrared (NIR) photodetectors have not been reported, because almost all photoactive materials which have NIR absorption inevitably absorb visible light. Nevertheless, the visible-blind NIR photodetectors have many unique applications, such as night vision systems and current fluorescence-based biomedical imaging.[19–21] They require a detector which can precisely discern emitted signals within as small as tens of

nanometers of wavelength difference, meanwhile excluding the background noise induced by tissue autofluorescence and excited signals. Moreover, biological tissues have strong visible light absorption, while having a transparency window in the long-wavelength range from 650 to 1450 nm for imaging.[22] Therefore, NIR-response narrow-band detectors with a small FWHM may provide a potential vision for accurate bioimaging.

A general strategy to meet these application requirements is to combine band-pass filters with sensitive broad-band photodetectors; however, this comes with some limitations. For instance, they suffer from high cost associated with the optical filters as well as the complicated optical system integration and debugging. Moreover, current commercial band-pass filters, in many cases, are unable to meet the increasingly stringent application requirements due to their intrinsic limitations. For example, the bulky size of filters and optics make it difficult to integrate them into portable bio-sensors. Recently, a narrow-band long-wavelength photodetector with a sub-100 nm FWHM based on polymer/fullerene photodiodes was reported by manipulating the relationship between the light wavelength and charge collection lengths.[23] The external quantum efficiency (EQE) is less than 10% in the range of 900–1000 nm, because the major portion of carriers generated by NIR light has to be lost with those generated by visible light in order to retain the narrow-band response. The low responsivity may severely limit their applications.

In this work, we present a highly sensitive, filterless, visible-blind and narrow-band NIR photodetector with a FWHM of <50 nm, by employing the trapping effect of lead sulfide (PbS) quantum dots (QDs) to generate a photoconductive gain. The hole trap-induced multiple electron injection dramatically

Department of Mechanical and Materials Engineering, and Nebraska Center for Materials and Nanoscience, University of Nebraska–Lincoln, Lincoln, Nebraska 68588-0656, USA. E-mail: jhuang2@unl.edu

enhances both the device responsivity and the visible rejection ratio of EQE by >10 fold with a strongly suppressed responsivity in the visible range, enabling a directly measured noise equivalent power (NEP) of 6.13 pW cm^{-2} at 890 nm and a large linear dynamic range (LDR) of 110 dB.

2. Results and discussion

The device structure of our nanocomposite photodetector is schematically shown in Fig. 1a. Here, the poly[2,7-(5,5-bis-(3,7-dimethyloctyl)-5H-dithieno[3,2-b:2′,3′-d]pyran)-alt-4,7-(5,6-difluoro-2,1,3-benzothia diazole)] (PDTP-DFBT):[6,6]-phenyl C71 butyric acid methyl ester (PC$_{71}$BM) blend is termed the bulk-heterojunction photoactive layer, and lead sulfide (PbS) quantum dots (QDs) act as the hole-trap centre. Tin oxide (SnO$_2$) works as the electron transporting layer, combined with PEIE (polyethylenimine, 80% ethoxylated) to reduce its work function to −4.1 eV.[24,25] At the anode side, molybdenum trioxide (MoO$_3$) works as the hole transporting/electron blocking layer. The PbS QDs are well dispersed in the active layer, which is shown by the cross-sectional scanning electron micrograph (SEM) (Fig. 1b) and verified by mapping the distribution of Pb (Fig. 1c) and S (Fig. 1d) with energy-dispersive X-ray spectroscopy (EDX). Fig. 1e shows the absorption spectrum of the PbS QD films and 4 μm-thick blend films with or without PbS QDs added. It can be seen that PbS QDs have wide absorption spectra from the UV-visible to NIR range, accompanied by a peak around 900 nm. On the other hand, the absorption of 4 μm-thick blend films with or without PbS QDs drops sharply from 850 nm. The nanocomposite film with PbS QDs has a little bit higher absorption at wavelengths above 900 nm, which can be attributed to the absorption from the PbS QDs in this range. Visible light is completely absorbed due to the very thick polymer layer used, but NIR light can partially penetrate the device. The origin of narrowband photodetection in the NIR range is illustrated in Fig. 1f.[23,26] Shorter wavelength visible light is strongly absorbed, and the photogenerated carriers are generated close to the ITO side (blue line) due to the shorter penetration length (L_p) in the visible wavelength range. Since the active layer thickness is much larger than the sum of the L_p of visible light and the drift distance (L_{2d}) of holes, almost no holes can be collected by the Ag electrode which then end up with nonradiative recombination, and thus the devices have no response in the visible range. On the other hand, NIR light can penetrate much deeper into the active layer and generate free carriers closer to the Ag side (red line). These free charges have the chance to be collected by the Ag anode to yield the photocurrent, if their distance from the Ag electrode is less than the L_{2d}. Therefore, visible-blind and narrow-band NIR photodetection can be achieved without the need for any extra filters.

The first generation of such narrow-band photodetectors has limited sensitivity because most of the charges generated even in PbS cannot be collected and the photodetectors do not have a gain mechanism while working in the photodiode
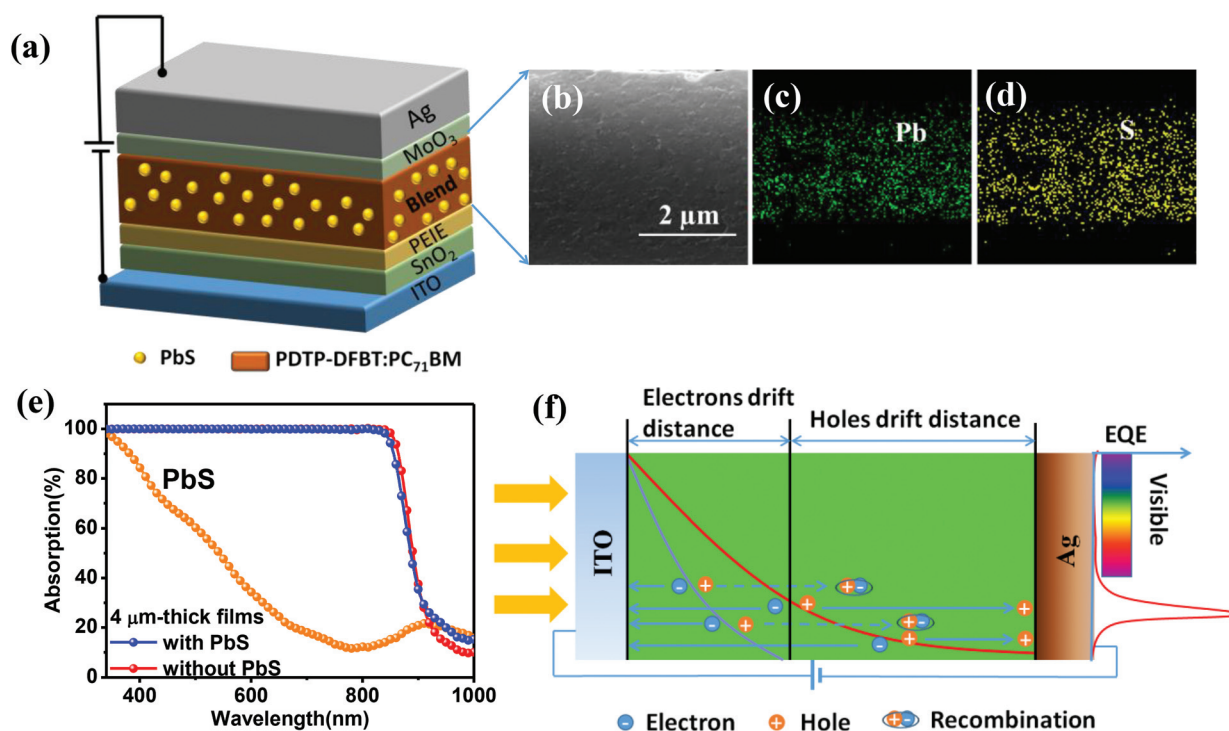

Fig. 1 (a) Device structure of the nanocomposite photodetectors. (b) Cross-sectional SEM of the active layer. Mapping of the distribution of Pb (c) and S (d) in the active layer with EDX. (e) Absorption spectra of PbS films, 4 μm thick PDTP-DFBT:PC$_{71}$BM films with or without PbS QDs added. (f) The illustration of the narrow-band NIR photodetector working mechanism.
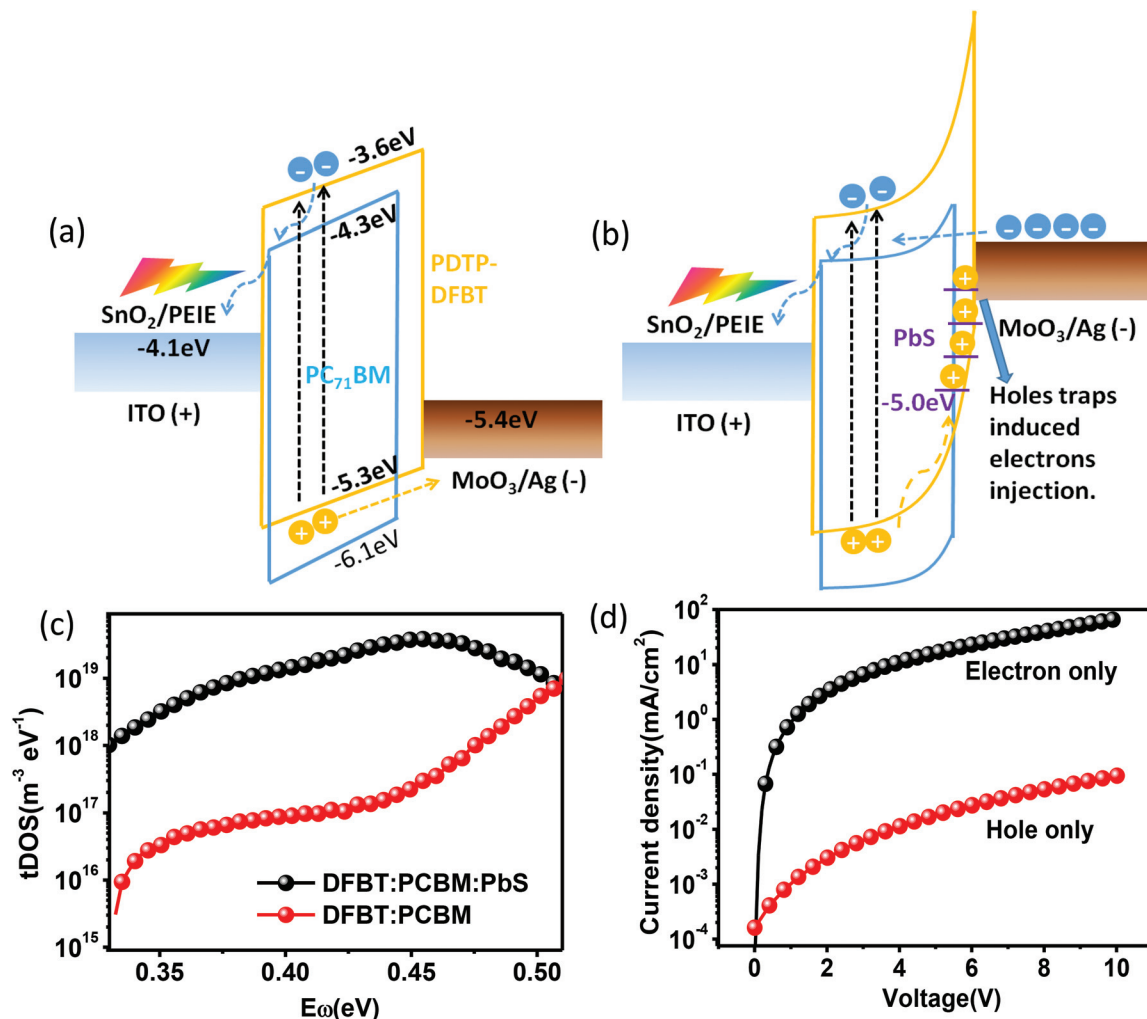
Fig. 2 The energy diagram of the photodetectors under illumination without (a) and with (b) PbS QD traps. (c) The trap density of states *versus* demarcation energy for the devices with or without PbS QDs. (d) *J–V* curves of the single-carrier (electron-only and hole-only) devices in the dark.

mode (Fig. 2a). Here we introduce the photoconductive gain to improve the responsivity of the narrow band gap photodetectors, which is illustrated in Fig. 2b. In these new devices, the added PbS QDs were chosen to have a strong hole trapping capability. These nanocomposite devices still operate as a photodiode in the dark due to the large energy barrier for charge injection under reverse bias. Under illumination, as shown in Fig. 2b, the incident photon generated holes in the vicinity of the anode were partially trapped by the low band gap discrete PbS QDs. The accumulated holes close to the anode shift the highest occupied molecular orbital (HOMO) level of the PDTP-DFBT upwards, and align the Fermi energy of the active layer with that of the anode. This upward band bending makes the Schottky barrier thinner so that electrons can be easily injected into the active layer from the anode by tunnelling under the applied reverse bias. Therefore, the working mode is transformed from the photodiode to the photoconductor, if the electron recombination lifetime is significantly longer than the electron transit time, which yields

multi-cycle circulation of electrons in the device before the recombination. As a result, the photoconductive gain is introduced to the narrow-band photodetector.

To determine whether the traps were successfully introduced into the devices, and which type of charge is trapped, we performed thermal admittance spectroscopy (TAS) combined with space charge limited current (SCLC) measurement of the devices with and without PbS QDs. Fig. 2c shows the calculated trap density of states *versus* the function of demarcation energy resulting from the TAS measurement. It can be clearly seen that the introduction of PbS QDs significantly increased the trap density by two orders of magnitude, and the trap depth is below 0.47 eV. Fig. 2d shows the current density–voltage (*J–V*) characteristics of the hole-only and electron-only devices measured in the dark. The electron-only device and the hole-only device possess ITO/SnO$_2$/PDTP-DFBT:PC$_{71}$BM:PbS QDs/BCP/Ag and ITO/PEDOT/PDTP-DFBT:PC$_{71}$BM:PbS QDs/MoO$_3$/Ag structures, respectively. It is observed that the current density in the electron-only device of PDTP-DFBT:

$PC_{71}BM$:PbS QDs is at least 3 orders of magnitude higher than that of the hole-only device. The calculated electron and hole mobilities are 6.1×10^{-2} cm^2 V^{-1} s^{-1} and 6.8×10^{-5} cm^2 V^{-1} s^{-1}, respectively, which confirmed the strong trapping of holes by the PbS QDs in the nanocomposite layer, because PDTP-DFBT:$PC_{71}BM$ without PbS has balanced electron and hole transport.[27]

To determine the response wavelength as well as the responsivity, the EQE of the devices with and without PbS QDs were measured and compared as shown in Fig. 3a and b, respectively. A narrow-band response with a FWHM of <50 nm appears in the NIR range for both the devices in the EQE spectra. The onset of the EQE is around 850 nm, which is in accordance with the absorption cutoff of PDTP-DFBT:$PC_{71}BM$. Moreover, the introduction of PbS QDs dramatically increases the peak EQE at 890 nm by >10 folds from 15% to 183%. In a photodetector, an EQE value of 100% is equivalent to a photo-conductive gain value of unity. Therefore, an EQE value larger than 100% means that our photodetector is working in the photoconductive gain mode. The responsivity of the devices with PbS QDs is calculated to be 1.31 A W^{-1}, which is one order of magnitude larger than that (0.11 A W^{-1}) of the devices without PbS QDs.

In addition, it is noted that the visible rejection ratio, which is derived from the ratio of EQEs in the NIR range and in the visible range, were increased to >100 from the original

~10 after introducing PbS QDs, as shown in the insets of Fig. 3a and b. The maximum visible rejection ratio was increased to 470. This exciting phenomenon represents a substantial advance compared to our previous results.[26] It can be attributed to again the difference of the collection efficiency for the charges generated by different wavelengths. As described above, there must be trapping of photo-generated holes at the interface of the nanocomposite/cathode to trigger the secondary electron injection and thus induce the gain. The holes generated by the incident visible photons cannot survive the transport to the trapping sites at the affinity of the cathode, and thus there is the absence of gain for the photons in the visible range. On the contrary, holes generated by NIR light deep in the film have the chance to travel to the interface of the nanocomposite/MoO_3 to be trapped there, which enables trapped-hole-induced-electron injection and the gain in the NIR range. In addition, the stronger NIR absorption of PbS QDs, which matches well with the tail-state absorption of polymer-fullerene, also contributed to the enhanced EQE in the NIR range, even in the absence of an applied field. Meanwhile, we found that 4 μm is the optimal thickness of the absorbing layer to suppress the visible light response and thus to achieve a visible–blind feature. The narrow-band response is sensitive to the film thickness. The photodetector with a less than 4 μm active layer showed a small visible response under bias, despite a higher NIR narrow-band response being
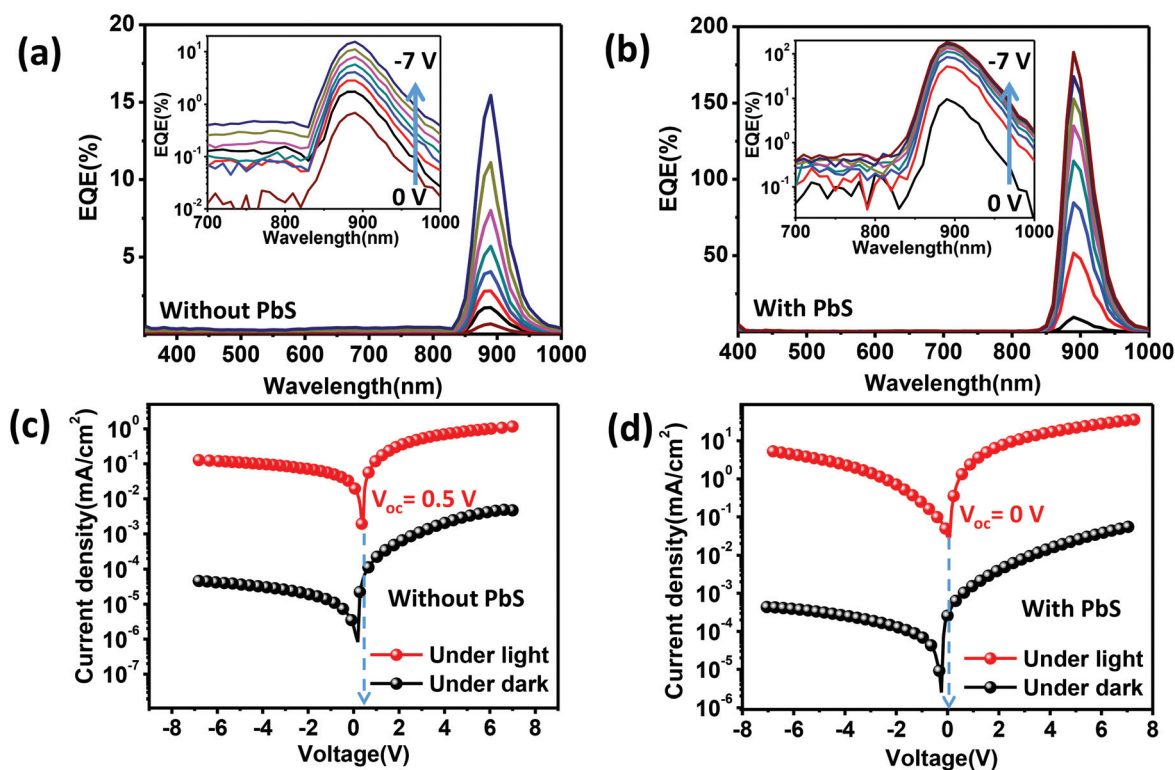

Fig. 3 (a, b) EQE spectra of the photodetectors without PbS QDs (a), and with PbS QDs (b) under reverse bias from 0 to −7 V with an interval of 1 V. Insets: EQEs under logarithmic coordinates. (c, d) The dark current and photocurrent (under simulated AM 1.5G irradiation) curves of the devices without PbS QDs (c) and with PbS QDs (d).

obtained. On the other hand, increasing the photoactive layer thickness to beyond 4 μm won't cause a visible response, but it reduces the device response.

The dark and photocurrent J–V characteristics were measured and shown in Fig. 3c and d. In the dark, it can be clearly seen that both the devices showed good rectification with a rectification ratio of >10^2 under ±7 V, indicating good diode behavior for both the devices. Under simulated AM 1.5G irradiation (100 mW cm^{-2}), the devices without PbS QDs showed a decreased rectification ratio to 10 under ±7 V, and a noticeable open circuit voltage (V_{oc}) of ~0.5 V, suggesting that the devices still work as a photodiode under light, which is consistent with the absence of the photoconductive gain in the EQE measurement. In contrast, the rectification ratio of the devices with PbS QDs drops to 7 without a notable V_{oc} under light. These observations support the devices with PbS QDs working in photoconductor mode under light.

In order to assess the sensitivity of both the photodetectors, a fast Fourier transform (FFT) signal analyzer combined with a current pre-amplifier was used to record their noise current at different frequencies under a bias of −7 V, and the results are shown in the inset of Fig. 4a. It is obvious that the flicker noise (1/f noise) is dominant in both the devices. The noise

current of the device with PbS QDs is slightly higher than that of the device without PbS QDs, which might be caused by the increased leakage current due to the aggregation of PbS QDs, as shown in Fig. 3c and d.[28] The relevant device performance parameters including responsivity (R), noise current (i_n), noise equivalent power (NEP), and specific detectivity ($D*$) can be calculated by using the following equations and the results are summarized in Table 1:[29]

$$D* = \frac{(AB)^{\frac{1}{2}}}{\text{NEP}} \left(\text{cm Hz}^{\frac{1}{2}} \text{W}^{-1} \text{ or Jones} \right) \quad (1)$$

$$\text{NEP} = \frac{i_n}{R} \left(\text{W Hz}^{-\frac{1}{2}} \right) \quad (2)$$

Table 1 Summary of the responsivity, noise current, noise equivalent power, specific detectivity of the devices with or without PbS QDs

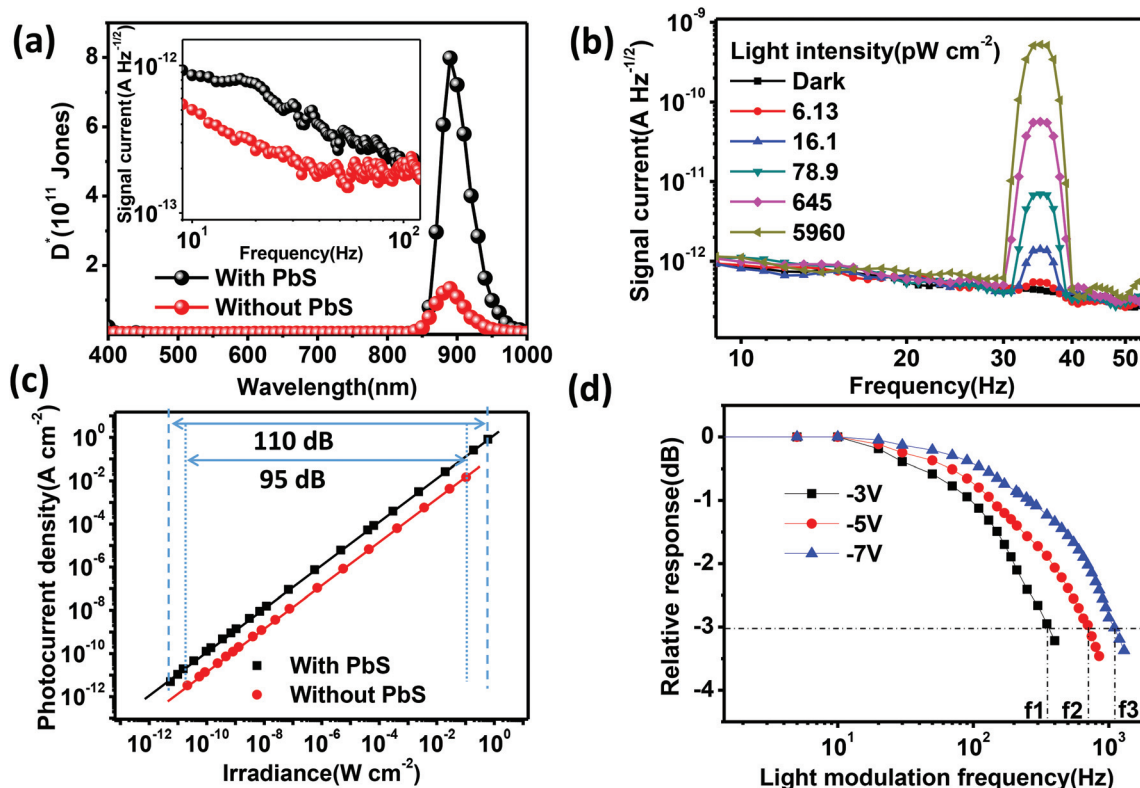| Device type	R (A W^{-1})	i_n@35 Hz (A Hz$^{-1/2}$)	NEP (W Hz$^{-1/2}$)	$D*$ (Jones)
With PbS	1.31	4.36×10^{-13}	3.33×10^{-13}	7.98×10^{11}
Without PbS	0.11	2.21×10^{-13}	2.01×10^{-12}	1.33×10^{11}

Fig. 4 (a) The specific detectivity of the photodetectors with and without PbS QDs at −7 V bias. The inset shows the noise spectra of these photodetectors with or without PbS QDs at −7 V bias. (b) The signal current spectra of the photodetectors with PbS QDs illuminated by an 890 nm LED modulated at 35 Hz with various light intensities realized by neutral density filters. (c) The dynamic response of the photodetectors with or without PbS QDs at −7 V bias under continuous LED illumination with various light intensities. The solid lines are linear fits to the data. (d) Normalized photocurrent under −3 V, −5 V, −7 V bias of the photodetector with PbS QDs versus the light modulation frequency of an 890 nm LED.

$$R = \frac{\text{EQE} \cdot e\lambda}{hc} \left(\text{A W}^{-1} \right) \quad (3)$$

where A is the device area (7 mm^2 in this work), B is the bandwidth, h is the Planck's constant, c is the light speed, and λ is the light wavelength. Also, as shown in Fig. 4a, D^* for the devices with PbS QDs at 35 Hz is 8.0×10^{11} Jones, which is dramatically enhanced compared to that of 1.3×10^{11} Jones for the devices without PbS QDs. This is mainly attributed to the increased responsivity by one order of magnitude enabled by the introduction of the photoconductive gain, regardless of a little increase in the noise current.

The NEP of photodetectors with PbS QDs is calculated to be 3.33×10^{-13} W Hz$^{-1/2}$, which suggests that the photodetectors should be able to detect the NIR light intensity of 4.75 pW cm^{-2} at 890 nm for a device with an area of 7 mm^2. Recently, a method to directly measure the lowest detectable light intensity of photodetectors was developed by us.[7,10,26,28,30] It can be used to verify whether photodetectors can actually detect light intensity as low as the calculated NEP. According to the definition of NEP, it represents the lowest detectable light intensity at which the signal of a photodetector cannot be differentiated from the noise current any more. The signal current of the devices under various light intensities was directly measured with the FFT signal analyzer in the same way as the noise current was measured, and the light intensity that causes the lowest distinguishable signal (shown as a red peak in Fig. 4b) is defined as the measured NEP. In this measurement, a NIR light-emitting diode (LED, electroluminescence peak at 890 nm) was employed as the light source and modulated at 35 Hz by an optical chopper. In Fig. 4b, the signal peaks manifest themselves on the measured current curves at 35 Hz, and their magnitude decreases with the reducing incident light intensity. The signal peak was buried in the background noise current when the light intensity went below 6.1 pW cm^{-2}, which is comparable to the calculated NEP from D^* (4.75 pW cm^{-2}).

To figure out whether the responsivity of the devices remains constant at various light intensities, the linear dynamic range (LDR) of the photodetector was measured by using a lock-in amplifier. Fig. 4c shows that the photocurrent of the devices with PbS QDs increases linearly with the light intensity from 6.1 pW cm^{-2} to 0.6 W cm^{-2}, yielding a large LDR of 110 dB with a linear response of 11 orders of magnitude, as defined by using the following equation:[29]

$$\text{LDR} = 10 \log \frac{P_{\text{sat}}}{\text{NEP}} \quad (4)$$

where P_{sat} is the light intensity causing the signal saturation. This LDR is among the largest values measured for polymer-fullerene based photodetectors, and it is comparable to that of the best Si photodetector (120 dB), and much higher than that of (66 dB) of conventional InGaAs photodetectors.[6] The LDR of the photodetectors without PbS QDs was also measured and is shown in Fig. 4c, which shows a LDR of 95 dB from 29.1 pW cm^{-2} to 0.11 W cm^{-2}. The nearly two orders of magnitude

improvement of the linear response can be attributed to the introduction of a photoconductive gain especially under weak light.

Finally, the response speed of the photodetectors with PbS QDs was measured by the $f_{-3\text{ dB}}$ method, and the result is shown in Fig. 4d. The devices were illuminated by the same NIR LED (890 nm) with varied turning on/off frequencies, and the photocurrent of the photodetectors was recorded by using a lock-in amplifier. The device response speed is strongly dependent on the reverse bias because of the changed carrier transit time as follows:[29]

$$f_{-3\text{ dB}} = \frac{0.35}{t_{\text{R}}} \quad (5)$$

where t_{R} is the response time of the devices. The 3 dB cut-off frequencies are $f_1 = 360$ Hz ($t_{\text{R1}} = 970$ μs), $f_2 = 700$ Hz ($t_{\text{R2}} = 500$ μs), and $f_3 = 1100$ Hz ($t_{\text{R3}} = 318$ μs) at −3 V, −5 V and −7 V, respectively.

3. Conclusion

In summary, we reported a highly sensitive, visible-blind, and narrow-band NIR photodetector with a FWHM of <50 nm and a visible rejection ratio >100. The PbS QDs were introduced as hole traps which successfully transformed the device working mode from the photodiode in the dark to the photoconductor under light, which leads to an improvement in both the responsivity and the visible rejection ratio by one order of magnitude. We believe that the NIR photodetectors with the directly measured NEP as low as 6.1 pW cm^{-2} and a larger LDR of 110 dB can find application in biological detection and biomedical imaging.

4. Experimental section

Materials preparation

Tin oxide (SnO$_2$) nanocrystalline QDs were prepared according to a reported method.[31] Poly[2,7-(5,5-bis-(3,7-dimethyloctyl)-5H-dithieno[3,2-b:2′,3′-d]pyran)-alt-4,7-(5,6-difluoro-2,1,3-benzothia diazole)] (PDTP-DFBT):[6,6]-phenyl C71 butyric acid methyl ester (PC$_{71}$BM) (1 : 2 in weight ratio) was dissolved in dichlorobenzene (DCB) with a concentration of 10 mg mL^{-1}, and stirred at 70 °C for 12 h before use. PEIE (polyethylenimine, 80% ethoxylated, $M_{\text{w}} \approx 70\,000$ g mol^{-1}, 35–40 wt% in H$_2$O) was purchased from Sigma-Aldrich, and was diluted with 2-methoxyethanol to a concentration of 0.4 wt%. PbS QDs (core size ~3 nm, 10 mg ml^{-1} in toluene) were purchased from Strem Chemicals, Inc. The toluene solvent was completely evaporated, and then, the PbS QDs were re-dispersed in the DCB solvent at a concentration of 10 mg ml^{-1}.

Device fabrication

SnO$_2$ solution was spun-coated on the top of pre-cleaned ITO substrates at a speed of 3500 rpm for 1 min, and annealed at

150 °C for 1 h in ambient air. This process was repeated 3–5 times to form compact SnO_2 films. Then, PEIE solution was spun-coated on the top of SnO_2 films at a rate of 5000 rpm for 1 min, and annealed at 100 °C for 10 min in ambient air. Next, the as-prepared blend solution of PDTP-DFBT:PC_{71}BM:PbS QDs $(1:2:0.2$ in weight ratio) were dropped on the PEIE films, and solvent-annealed for 16 h by placing the samples in the DCB solvent for 12 h. Finally, 10 nm MoO_3 and 100 nm Ag were thermally evaporated on top of the active layers in sequence. The device active area is 7 mm^2.

Measurement of the trap density of state

The distribution of the traps was characterized by calculating the trap density of states as a function of demarcation energy measured by thermal admittance spectroscopy (TAS).[32] The demarcation energy (E_ω) correlates with the frequency by:

$$E_\omega = k_B T \ln \frac{\omega_0}{\omega} \qquad (6)$$

where k_B is the Boltzmann constant, T is the absolute temperature, ω is the applied angular frequency, and ω_0 is the attempt to escape frequency, which is set at 10^9 kHz here. The distribution of trap density of states (N_T) can be calculated by using:

$$N_T(E_\omega) = -\frac{V}{d}\frac{dC}{d\omega}\frac{\omega}{k_B T} \qquad (7)$$

where V is the applied reverse bias, d is the film thickness, and q is the elementary charge.

Calculating the carriers' mobility

The carrier mobility was calculated using Child's law of space-charge limited current (SCLC):[33]

$$J = \frac{9}{8}\varepsilon_r \varepsilon_0 \mu \frac{V^2}{d^3} \qquad (8)$$

where ε_r is the relative dielectric constant, ε_0 is the permittivity of vacuum, μ is the charge carrier mobility, and V is the applied voltage.

Acknowledgements

References

1 X. Gong, M. Tong, Y. Xia, W. Cai, J. S. Moon, Y. Cao, G. Yu, C. L. Shieh, B. Nilsson and A. J. Heeger, *Science*, 2009, **325**, 1665.

2 H. Y. Chen, M. K. F. Lo, G. Yang, H. G. Monbouquette and Y. Yang, *Nat. Nanotechnol.*, 2008, **3**, 543.

3 F. Guo, B. Yang, Y. Yuan, Z. Xiao, Q. Dong, Y. Bi and J. Huang, *Nat. Nanotechnol.*, 2012, **7**, 798.

4 S. A. McDonald, G. Konstantatos, S. Zhang, P. W. Cyr, E. J. Klem, L. Levina and E. H. Sargent, *Nat. Mater.*, 2005, **4**, 138.

5 G. Konstantatos, M. Badioli, L. Gaudreau, J. Osmond, M. Bernechea, F. P. G. de Arquer, F. Gatti and F. H. L. Koppens, *Nat. Nanotechnol.*, 2012, **7**, 363.

6 L. Dou, Y. Yang, J. You, Z. Hong, W.-H. Chang, G. Li and Y. Yang, *Nat. Commun.*, 2014, **5**, 5404.

7 L. Zhang, T. Yang, L. Shen, Y. Fang, L. Dang, N. Zhou, X. Guo, Z. Hong, Y. Yang, H. Wu, J. Huang and Y. Liang, *Adv. Mater.*, 2015, **27**, 6496.

8 J. Qi, X. Zhou, D. Yang, W. Qiao, D. Ma and Z. Wang, *Adv. Funct. Mater.*, 2014, **24**, 7605.

9 Y. Yao, Y. Liang, V. Shrotriya, S. Xiao, L. Yu and Y. Yang, *Adv. Mater.*, 2007, **19**, 3979.

10 R. Dong, Y. Fang, J. Chae, J. Dai, Z. Xiao, Q. Dong, Y. Yuan, A. Centrone, X. Zeng and J. Huang, *Adv. Mater.*, 2015, **27**, 1912.

11 Y. Rim, Y. Yang, S.-H. Bae, H. Chen, C. Li and M. S. Goorsky, *Adv. Mater.*, 2015, **27**, 6885.

12 Q. Lin, A. Armin, D. M. Lyons, P. L. Burn and P. Meredith, *Adv. Mater.*, 2015, **27**, 2060.

13 K. Manga, J. Wang, M. Lin, J. Zhang, M. Nesladek, V. Nalla, W. JI and K. Loh, *Adv. Mater.*, 2012, **24**, 1697.

14 X. Zhou, D. Yang and D. Ma, *Adv. Opt. Mater.*, 2015, **3**, 1570.

15 J. Yumoto, H. Yajima, Y. Seki, J. Shimada and M. Nakajima, *Appl. Phys. Lett.*, 1982, **40**, 632.

16 O. Katz, V. Garber, B. Meyler, G. Bahir and J. Salzman, *Appl. Phys. Lett.*, 2001, **79**, 1417.

17 K. J. Bachmann and J. L. Shay, *Appl. Phys. Lett.*, 1978, **32**, 446.

18 S. Ghosh, C. Rivera, J. L. Pau, E. Munoz and O. Brandt, *Appl. Phys. Lett.*, 2007, **90**, 091110.

19 J. E. Källhammer, *Nat. Photonics*, 2006, Sample issue, 12.

20 Z. Guo, S. Park, J. Yoon and I. Shin, *Chem. Soc. Rev.*, 2014, **43**, 16.

21 J. Chen, W. Liu, B. Zhou, G. Niu, H. Zhang, J. Wu, Y. Wang, W. Ju and P. Wang, *J. Org. Chem.*, 2013, **78**, 6121.

22 R. Wang and F. Zhang, *J. Mater. Chem. B*, 2014, **2**, 2422.

23 A. Armin, R. D. J. Vuuren, N. Kopidakis, P. L. Burn and P. Meredith, *Nat. Commun.*, 2015, **6**, 6343.

24 Y. Zhou, C. Hernandez, J. Shim, J. Meyer, A. J. Giordano, H. Li, P. Winget, T. Papadopoulos, H. Cheun, J. Kim, M. Fenoll, A. Dindar, W. Haske, E. Najafabadi, T. M. Khan, H. Sojoudi, S. Barlow, S. Graham, J. L. Bredas, S. R. Marder, A. Kahn and B. Kippelen, *Science*, 2012, **336**, 327.

25 I. Kim, X. Li, M. Ullah, P. E. Shaw, R. Wawrzinek, E. B. Namdas and S.-C. Lo, *Adv. Mater.*, 2015, **27**, 6390–6395.

26 L. Shen, Y. Fang, H. Wei, Y. Yuan and J. Huang, *Adv. Mater.*, 2016, **28**, 2043.

27 J. You, L. Dou, K. Yoshimura, T. Kato, K. Ohya, T. Moriarty, K. Emery, C.-C. Chen, J. Gao, G. Li and Y. Yang, *Nat. Commun.*, 2013, **4**, 1446.

28 Y. Fang and J. Huang, *Adv. Mater.*, 2015, **27**, 2804–2810.

29 *Photonic Devices*, ed. J.-M. Liu, Cambridge University Press, Cambridge, UK, 2005.

30 H. Wei, Y. Fang, Y. Yuan, L. Shen and J. Huang, *Adv. Mater.*, 2015, **27**, 4975.

31 B. Bob, T. Song, C.-C. Chen, Z. Xu and Y. Yang, *Chem. Mater.*, 2013, **25**, 4725.

32 J. A. Carr and S. Chaudhary, *Energy Environ. Sci.*, 2013, **6**, 414.

33 *Current injection in solids*, ed. M. A. Lampert and P. Mark, Academic Press, New York, 1970.